Dust sampling in WEST and tritium retention in tokamak-relevant tungsten particles

S. Peillon, G. Dougniaux, M. Payet, E. Bernard, G. Pieters, S. Feuillastre, S. Garcia-Argote, F. Gensdarmes, C. Arnas, F. Miserque, et al.

Nuclear Materials and Energy 24 (2020) 100781

Contents lists available at ScienceDirect

Nuclear Materials and Energy

journal homepage: www.elsevier.com/locate/nme

Dust sampling in WEST and tritium retention in tokamak-relevant tungsten particles

S. Peillon[a,g,*], G. Dougniaux[a], M. Payet[b], E. Bernard[b], G. Pieters[c], S. Feuillastre[c], S. Garcia-Argote[c], F. Gensdarmes[a], C. Arnas[d], F. Miserque[e], N. Herlin-Boime[f], C. Grisolia[b], O. Pluchery[g]

[a] Institut de Radioprotection et de Sûreté Nucléaire (IRSN), PSN-RES, SCA, Gif-sur-Yvette 91192, France
[b] CEA, IRFM, F-13108 Saint Paul lez Durance, France
[c] CEA Saclay, JOLIOT, Gif-sur-Yvette, France
[d] CNRS, Aix-Marseille université, PIIM, 13397 Marseille, France
[e] CEA Saclay, DEN – Service de la Corrosion et du Comportement des Matériaux dans leur Environnement (SCCME), Université Paris-Saclay, F-91191 Gif-sur-Yvette, France
[f] CEA Saclay, DRF/IRAMIS//NIMBE/LEDNA, Université Paris Saclay, F-91191 Gif-sur-Yvette, France
[g] Sorbonne Université, UPMC-CNRS, Institut des Nanosciences de Paris, France

ARTICLE INFO

Keywords:
Tokamak
WEST
Dust
Tritium
Tungsten
Adhesion

ABSTRACT

The paper presents complementary approaches based on experimental and numerical works to address the behavior of tokamak-relevant tungsten particles loaded with tritium. Sampling of particles inside the WEST tokamak have been realized thanks to an *in situ* particle collection system called Duster Box. This method allowed to identify various types of tungsten particles among them spherical shaped micro-particles between 5 μm and 30 μm in diameter. Based on these results a surrogate tungsten powder has been provided by means of spheroidization process and sieving method. Moreover, the powder tritium retention capacity was measured and specific activities of 90 MBq.g^{-1} and 280 MBq.g^{-1} were obtained for particles with 17 μm and 11.5 μm median diameters, respectively. Considering such tritium activities trapped in the particles, Monte-Carlo simulation were performed to estimate the electrostatic self-charging rates and the corresponding electrical charge carried by the radioactive tungsten dust. The results of these experiments provide robust data for the assessment of the dispersion of toxic/radioactive material in the environment that could follow a loss of containment.

1. Introduction

Due to the nature of its operation, a fusion facility generates dust by plasma-surface interaction that causes significant erosion of the vacuum vessel (VV) and the plasma-facing components (PFCs). Operators of the next generation of tokamaks will so have to manage hundreds of kilograms of dusts in the VV [1]. Characterization of the behavior of these dusts and especially the amount that can be re-suspended or are already airborne during normal operations is of major interest for the design and the definition of the operational procedure of the facility. Dust particles with a large range of sizes (from nm to cm), shapes and chemical compositions will be present in the VV due to the very specific conditions of their generation [2]. Therefore, it is necessary to know *a priori* the adhesive properties of these particles on the PFCs, in particular to evaluate their possible re-suspension and its consequences for the operating conditions of the plasma and on maintenance operations and their logistics.

When a plasma inside the tokamak is produced from isotopes of hydrogen (D and T), it must be considered that the materials present in the vacuum chamber (essentially alloys of tungsten, beryllium and steel but also metal oxides, carbides and hydride metals) will trap and retain large quantities of tritium according to their nature [3,4]. During plasma wall interaction, these plasma-facing material can be sputtered. The eroded material can be then transported and form co-deposited layers incorporating part of the radionuclides coming from the fuel of the discharges. Moreover, these layers are highly unstable due to high internal stresses. They can break easily during plasma operation leading to the creation of dust of (usually) large size [5]. In current machines, not all the co-deposited material is converted to dust and a conversion factor has been introduced [6]. However, the conversion factor from

* Corresponding author.
E-mail address: samuel.peillon@irsn.fr (S. Peillon).

https://doi.org/10.1016/j.nme.2020.100781
Received 21 January 2020; Received in revised form 17 July 2020; Accepted 20 July 2020
Available online 02 August 2020

eroded material to dust could be as low as 10 to 20% [6]. These observations will be the same with PFCs of low Z material and same results of layer delamination should be considered in case of beryllium deposited layers originating from PFC interaction with plasma.

With W PFCs and due to a lower sputtering yield, the dust production is supposed to be reduced. However, it has to be emphasized here that this phenomenon can be largely underestimated due to several processes. Among them is the boosted erosion of W due to its enhanced sputtering yield when the material temperature reaches 1400 K. This temperature value is closed to the PFC temperature expected in a large fusion reactor and a W sputtering yield of 1.5×10^{-4} atom/ion has been measured for such temperature in a 5 eV dense plasma [7]. Moreover, erosion processes may also lead to the production of particles due to accretion of eroded material in the low temperature plasma edge of a large tokamak such as ITER [8]. For W PFCs, preliminary laboratory results have evidenced the production of small and highly porous dust of several hundred nanometers [9]. This production process occurs when a tungsten target is sputtered by pure argon plasma during hundreds of second. In addition, production of dust is likely to occur for high energetic events such as impact of high energetic particles during disruption, arcing, Vertical Displacement Event (VDE), Edge Localized Modes (ELMs) and Runaway Electron phenomenon. Up to now, the dust production evaluation during all these events has not been studied carefully. This comes from several points. First of all, it is difficult to distinguish, in the collected dust, those coming from erosion and layer delamination to those coming from other processes. Therefore one relies on laboratory experiment as plasma gun interaction [10] or arc induced erosion [11] to predict erosion under ELMs, disruption or arcing processes. Finally, the production of dust during maintenance activities should not to be neglected. Indeed, dust will be produced during maintenance operations or during divertor cassette replacement when cutting and machining is used. In this case, dust will be of large size (several tens of micrometers) but have to be integrated in the global dust inventory.

For fine dust particles (below 100 μm), the adhesion forces of intermolecular attraction (van der Waals) generally exceed the other forces (e.g. gravity) by several orders of magnitude. While the main force of adhesion is the van der Waals force, other forces such as electrostatic forces triggered by the self-charging due to radioactivity of the particles, can arise [12]. Indeed, the self-charging of activated dusts and their re-suspension in electrostatic fields has already been proved while remaining strictly qualitative [13].

In order to gain knowledge on the dust resulting from the plasma-wall interaction, we collected particles in an existing tokamak. Therefore, Section 2 of the manuscript will present the sampling device used in the WEST tokamak [14] with tungsten PFCs. Examples of dust found in the VV after the second plasma campaign will be introduced. Based on these samples, the Section 3 of the paper will focus on the definition of a surrogate tungsten powder in order to perform tritium charging experiments under laboratory conditions. The experimental protocol to introduce tritium in the powder and the amount that can be trapped will be also addressed. Finally, Section 4 will introduce Monte-Carlo (MC) simulations performed to estimate the electrostatic self-charging rates of the tungsten spherical particles. Based on the simulation results, an analytical comparison between the electrostatic image force triggered by the β-decay of trapped tritium atoms in the dust particles with the van der Waals adhesion force is presented.

2. WEST sampling campaign

Many techniques are available for the sampling of dust deposited on the tokamak PFCs. Vacuuming is the most common technique and it has been used in pioneering work in the JET [15], DIII-D [16] and Textor-94 [17] tokamaks. Vacuuming is almost systematically performed after plasma campaigns nowadays and has been commonly used in the MAST [18] and ASDEX Upgrade [19] tokamaks. It is now permanently implemented in JET using a robotic arm equipped with a suction system (see Refs. [20–22]). This collection method has the advantage of being simple to implement and allows samples to be taken from large areas. On the other hand, it is difficult to correlate the characteristics of the collected particles with their positions in the machine. Another commonly used method, which has the advantage of being localized, is to dab the surfaces or visible dust deposits with a carbon tape mounted on electron microscopy supports. This method has been implemented in most tokamaks [23] but has several drawbacks: a force is applied to the surfaces which can tear off the co-deposited layers and break up the collected dust grains; the visible part of the collected dust is the underside and their morphology can be difficult to analyse since they are trapped in glue. To avoid using mechanical action, electrostatic detachment methods have also been proposed but remain difficult to implement in a tokamak environment [24,25]. A last method recently implemented in ASDEX Upgrade [26] and in JET [27] is to place in the vacuum chamber silicon plates to collect particles by sedimentation/impaction or diffusion during the plasma shots. This method has the advantage of being localized and without any action that could deteriorate the particles that settle on the silicon wafers. However, it is necessary to permanently integrate these plates in various places of the vacuum chamber which can be restrictive for other devices and equipment already numerous in actively cooled fusion machines like WEST.

In recent work, our team has used a small sampling device named Duster Box to collect dust by a controlled air flow in Tore Supra (with carbon PFCs) [28] and ASDEX Upgrade (tungsten PFCs) [29] tokamaks. The advantage of this collection technique is to investigate various locations of the PFCs surfaces, including collection on divertor targets, and to provide data corresponding to particles potentially mobilizable by airflow. Unlike suction nozzles used with the vacuuming technique, the Duster Box channel has been designed to act as an aerodynamic probe with well-defined and repeatable airflows. Indeed, when vacuuming, airflow velocities applied to detach particles are unknown since the distance from the surface, geometry of the nozzle and pressure drop in the aeraulic circuit are most of the time not qualified or without any information on their repeatability. Thus, the overall sampling efficiencies of such devices are not known with respect to airflow velocities and particle sizes. To increase the collection efficiency of such apparatus, it is common to add a brush to the suction nozzle in order to detach as much dust as possible. By doing so, one loses all informations on the aerodynamic forces needed to detach real tokamak particle deposits and representativeness for mobilizable particle by airflow. One should notice that these informations are mandatory for safety studies concerning the loss of vacuum accident (LOVA) where highly transient flows are expected to resuspend most of the dust present in the vacuum vessel. Previous experimental [30] and numerical work [31,32] about LOVA event have already demonstrated that friction velocities of few $m.s^{-1}$ are sufficient to aerosolize in the vacuum vessel tungsten particles in the micrometer range. By using a qualified aerodynamic probe such as the Duster Box device, one can identify, *a posteriori*, specific types of dust that are likely to detach in case of air ingress in the machine. The operating airflow of the Duster Box was set to 120 $l.min^{-1}$ during the sampling campaign in WEST. For such a flow, the friction velocity inside the sampling channel in contact with the PFCs components is 2.5 $m.s^{-1}$ which is close to the friction velocities values expected at the bottom of a large tokamak a few seconds after a LOVA [32]. The following section describes the device and its use for dust sampling in the WEST tokamak.

2.1. Dust sampling strategy

Nine dust samplings were realized in total on several locations of the lower divertor and the baffle of WEST after the second plasma campaign (C2 campaign). During this period, 716 plasmas were produced for a total duration of 1553 s (approximately 26 min of

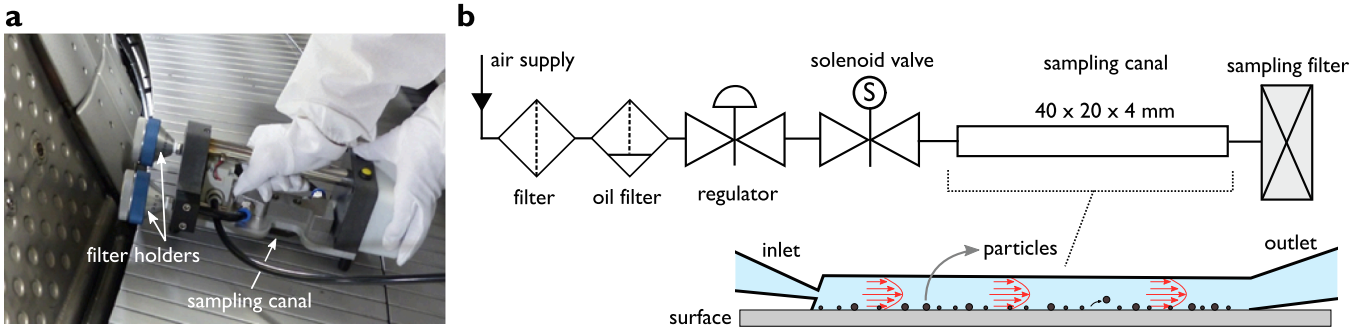

Fig. 1. a Close-up view of a sampling with the Duster Box on an inertially cooled PFU of the WEST lower divertor. **b** Aeraulic diagram of the Duster Box device.

cumulative plasmas). The number of disruptions in the vacuum chamber was 282 for this campaign.

A part of the lower divertor is composed of tungsten plasma-facing units (PFUs), 440 mm long, made of 35 tungsten ITER-like monoblocks (exposed surface is 12 × 26 mm) with a gap of approximately 0.5 mm between each of them. The other part is composed of graphitic PFUs coated with tungsten (inertially cooled PFUs) while the baffle is composed of copper fingers coated with tungsten. During the C2 campaign, camera videos have shown the effects of a runaway electron (RE) production during disruptions. A large number of droplets of molten metal was emitted from a "vertical" antenna protector limiter (LPA) under RE bombardment. Therefore, several dust samplings were performed on the baffle located below and near the LPA made of graphitic tiles covered by molybdenum interlayers and tungsten external coatings. Other dust samplings were performed on inertially cooled and ITER-like PFUs. Fig. 1**a** shows a photography of a sampling with the Duster Box on an inertially cooled PFU of the lower divertor.

2.2. Description of the sampling device

The device is a very small rectangular duct in which a calibrated airflow is drawn. The current version of the device produced friction velocities ranging between 0.1 m.s^{-1} to 3 m.s^{-1} inside the sampling channel. The principle is to inject clean dry compressed air (from 0.5 to 2 bars) into the channel through a slit of a few millimeters. The channel size has a sampling area of 20 × 40 mm^2 and a height of 4 mm. The compressed air is injected through a slit of 1 × 15 mm^2 forming an angle of 30° with the surface as depicted in Fig. 1**b**. This geometry has shown best results in terms of particle detachment [33]. The inlet pressurized clean air is controlled with the help of a solenoid valve and a pressure regulator. The flow can be continuous or pulsed with controlled opening time thanks to an Arduino card that drives the solenoid valve. Detached particles are collected on two 47 mm diameter filters installed downstream of the channel.

The filters used are Fluoropore^{TM} PTFE (Polytetrafluoroethylene) membranes with 3 μm pore size from the brand Millipore (ref. FSLW04700). These filters are known to have a reasonable pressure drop even at high airflow rates [34,35] and excellent average front-surface collection efficiency (CE > 99.5%). Due to their physical structure made of three distinct layers, the gas is forced to follow an irregular path through the complex pore structure [36]. The most penetrating particle size for this type of filter is between 20 nm and 100 nm where the collection efficiency drops to 92% for the nominal face-velocity of 0.4 m.s^{-1}. The collection efficiency of these PTFE membranes come back to 99.9% when the particle size is 300 nm and above [37]. Having maximum flow rate of 120 l.min^{-1} in the Duster Box, which corresponds to a face velocity of 1.15 m.s^{-1} for one filter (47 mm in diameter), we have implemented two filter holders in parallel to reduce the face velocity to 0.58 m.s^{-1} on each filter. These filter holders are visible in Fig. 1**a** at the outlet of the Duster Box device.

2.3. Origins and characterization of the collected dust

The filters used in the Duster Box for the sampling where analyzed by means of scanning electron microscope (SEM) and Energy Dispersive X-ray Spectroscopy (EDS) with a JEOL JSM-6010. Whatever the probed location, spherical particles of tungsten, stainless steel, molybdenum and silver as well as dust of irregular shape coming from the coating delamination were observed. In total, 58 particles were observed with SEM and 24 of them show a spherical geometry. The typical size of spherical particles resulting of the emission of molten material droplets is in the range 5–30 μm. The presence of spherical dust of tungsten and molybdenum was attributed to off-normal events mainly due to the impact of REs near the LPA. The presence of stainless-steel spherical dust was attributed to local melting on the first wall probably during arcing while silver-based dust could come from the protections of the ICRH (Ions Cyclotron Resonance Heating) antennas. SEM micrographs of Fig. 2**a** and d show typical tungsten spherical dust with diameters between 10 and 15 μm. Fig. 2**b** shows a molybdenum spherical particle 10 μm in diameter with a granular appearance at the surface. In WEST, molybdenum is used as an interlayer below the tungsten coatings to insure good joining with the carbon tiles [38]. Fig. 2**c** presents a tungsten bubble of approximately 22 μm likely coming from the tungsten boiling. Such bubbles have also been observed in JET but with smaller sizes [22]. The lower part of Fig. 2**e** shows a spherical tungsten microparticle of ~70 μm in diameter. Let us notice that large spherical particles produced from tungsten melting had already been observed in the TEXTOR-94 tokamak [17]. The author suggested that the perfectly spherical shape of these particles signified a solidification far from the walls after the melting of the metal by an electric arc or a disruption. It should be recalled that the formation of electric arcs has been considered for several years as a major source of impurities when the walls of the vacuum vessel are metallic [39]. This process of spherical tungsten particles formation by electric arcs has also been illustrated in ASDEX Upgrade [26]. The particle size distribution established by the authors at the end of the plasma campaign of 2009 revealed a mean size of ~1 μm and a maximum of ~30 μm [19]. Spherical tungsten particles were also observed in JET. In this case, there was no statistical study on the particle's sizes but published SEM images have shown a size range of 2–20 μm [27]. In Fig. 2**e**, left to the tungsten sphere, a piece of tungsten with a thickness of ~10 μm consistent with the tungsten coating on inertial PFCs is visible. The upper part of Fig. 2**e** shows a stainless-steel chunk (120 μm in length) that has been torn off the first wall. The compositions of this dust and the one of the sphere are given at the bottom of Fig. 2**e**.

This section has demonstrated that spherical tungsten particles of several micrometers in diameter are present in the WEST tokamak. These particles can be dense (full) or hollow like bubbles (shell with empty core). The next section focuses on powders that will be used in the laboratory to simulate the spherical tungsten particles found in WEST and other fusion machines such as ASDEX Upgrade [19] and JET [22]. Indeed, the amount of particles collected during the sampling

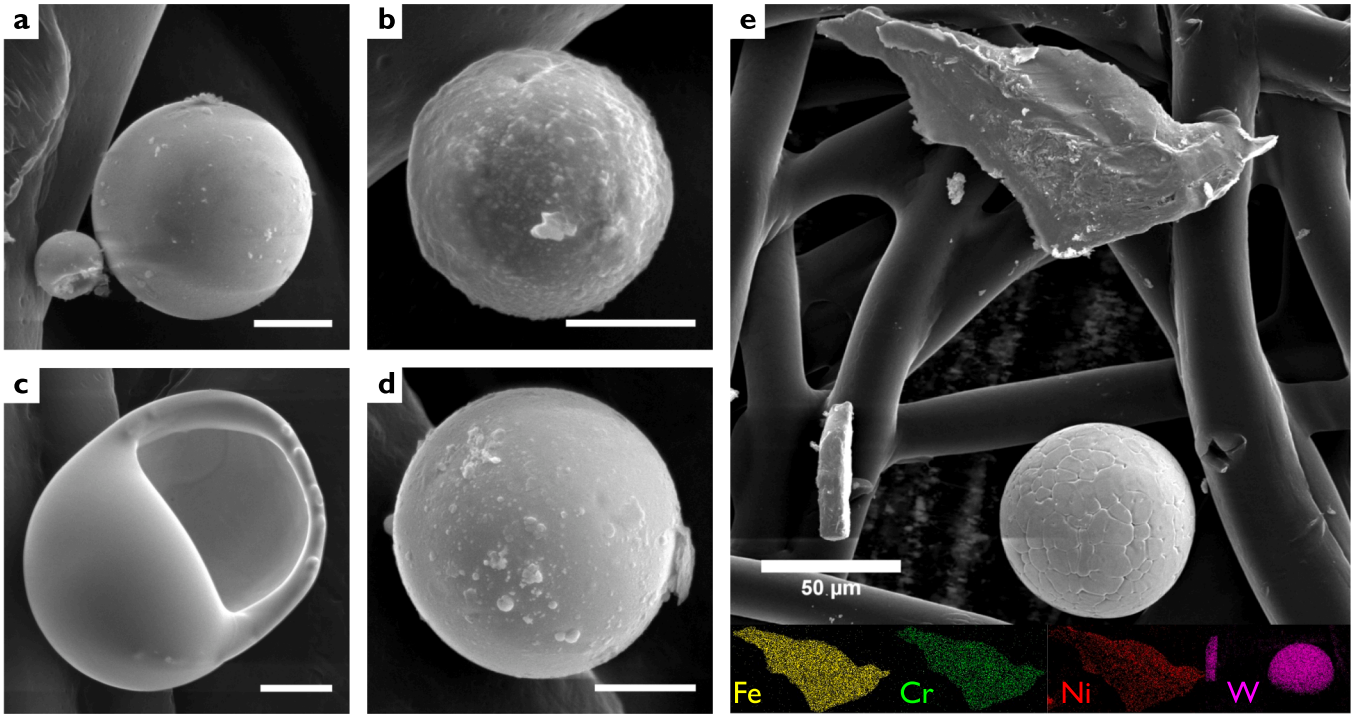

Fig. 2. **a** to **d** SEM micrographs of particles collected with the Duster Box inside the WEST tokamak (scale bars are 5 µm). **e** SEM and EDS analysis of stainless steel and tungsten particles deposited on a sampling filter.

campaign was very low thus preventing the use of these particles for other experiments than scanning electron microscopy (SEM) analysis.

3. Tritium charging

3.1. Definition of a tungsten powder surrogate

Two tungsten powders have been supplied for our experiments. The first one is marketed by the company *Tekna Advanced Materials Inc*. This W25 tungsten powder has undergone a spheroidization process [40] which allows to obtain large amount of spherical particles in the range 1–50 µm. These particles were then sieved at our laboratory using mesh sizes of 20 µm, 15 µm, and 5 µm. Before sieving, they were dispersed in a beaker containing ethanol and sonicated for 2 min before being poured onto the first sieve. The sieving column is then stirred for 30 min. The different sieves are recovered and dried (40 °C) for several hours. The dried particles are then recovered in pill containers using brushes. This procedure eliminates the largest ones (diameters greater than 20 µm) and aggregates and provides a powder with a reduced particle size distribution whose mass median diameter is 17 µm with a geometric standard deviation of 1.52. The second tungsten powder was purchased from *Alfa Aesar* and sent to *Tekna Advanced Materials Inc*. for spheroidization. This second powder, denoted AF5 in the following, has experienced the same sieving protocol as W25 tungsten powder. Its mass median diameter is 11.5 µm with a geometric standard deviation of 1.63. Fig. 3**a** and b show the normalized volume particle size distributions of the W25 and AF5 powders before and after the sieving procedure. These particle size distributions (PSD) were obtained and analyzed with a PSD-3603 AEROSIZER® from TSI. The insert in Fig. 3**a** shows a SEM micrograph of a W25 sieved sample composed of spherical particles with diameters between 10 µm and 20 µm. The particle size distributions of Fig. 3 show a clear effect of the sieving procedure by reducing the geometric median diameter and the width of the distribution. The AF5 particle size distribution shows a greater dispersion in particle sizes but with smaller diameters.

An XPS (X-ray Photoelectron Spectroscopy) analysis has been carried out on the stock W25 powder with a ThermoFisher ESCALAB 250xi equipped with a monochromatized Al-K_α X-ray source ($h\nu$ = 1486.6 eV). A 20 eV pass energy has been chosen for high resolution acquisition together with the commercial Avantage® software for the fitting procedure as previously described in [41]. The W-4f core-levels spectrum obtained is presented in Fig. 3**c**. This spectrum was recomposed using 4 doublets (spin coupling $4f_{5/2}$ – $4f_{7/2}$) [41].

For all contributions, we found that the $4f_{5/2}$ – $4f_{7/2}$ doublet separation is fixed at 2.2 eV with area ratios also fixed at 3:4. These contributions are attributed to metallic tungsten W (orange in Fig. 3**c**) with binding energies of 31.0 eV and 33.2 eV for W-$4f_{7/2}$ and W-$4f_{5/2}$ core levels, respectively. Presence of W-4f in WO_x ($x < 2$) was revealed by the two peaks at 31.7 eV and 33.9 eV (green in Fig. 3**c**) and a quite low contribution of WO_2 (dark blue) was found with $4f_{7/2}$ and $4f_{5/2}$ located at 32.4 eV and 35.5 eV. Finally, a large contribution of WO_3 (light blue in Fig. 3**c**) was found at 35.6 eV and 37.8 eV for the W-$4f_{7/2}$ and W-$4f_{5/2}$ core levels [42].

True density of each batch was determined with a Helium Pycnometer ACCUPYC1330 and a cell of 10 cm^3 in volume. Prior to measurement, outgassing of the samples was performed at 130 °C for several hours in air in order to remove any adsorbed water layer. Density obtained after 50 measurements are ρ_{W25} = 18820 ± 20 $kg.m^{-3}$ and ρ_{AF5} = 18725 ± 50 $kg.m^{-3}$ for W25 and AF5 powders, respectively. To estimate the thickness of the tungsten oxide layer we have considered a simple core/shell structured particle with a core density equal to the tungsten bulk (ρ_{core} = 19300 $kg.m^{-3}$) and a shell density equal to the tungsten trioxide density, i.e., ρ_{shell} = 7160 $kg.m^{-3}$. For the particles of 17 µm in diameter of the W25 powder, this corresponds to a shell thickness of ~110 ± 5 nm which represents ~4% of WO_3 in volume for such spherical particle. For the 11.5 µm particles of the AF5 powder, one finds a shell thickness of ~90 ± 5 nm. Since metallic tungsten is observed in the information depth of XPS (Fig. 3**c**), these values given above are an upper limit for the WO_3 shell thickness. Furthermore, impurities present during the He pycnometry measurements may have artificially increased the sampled volume thus reducing the density of the powder. Such calculation

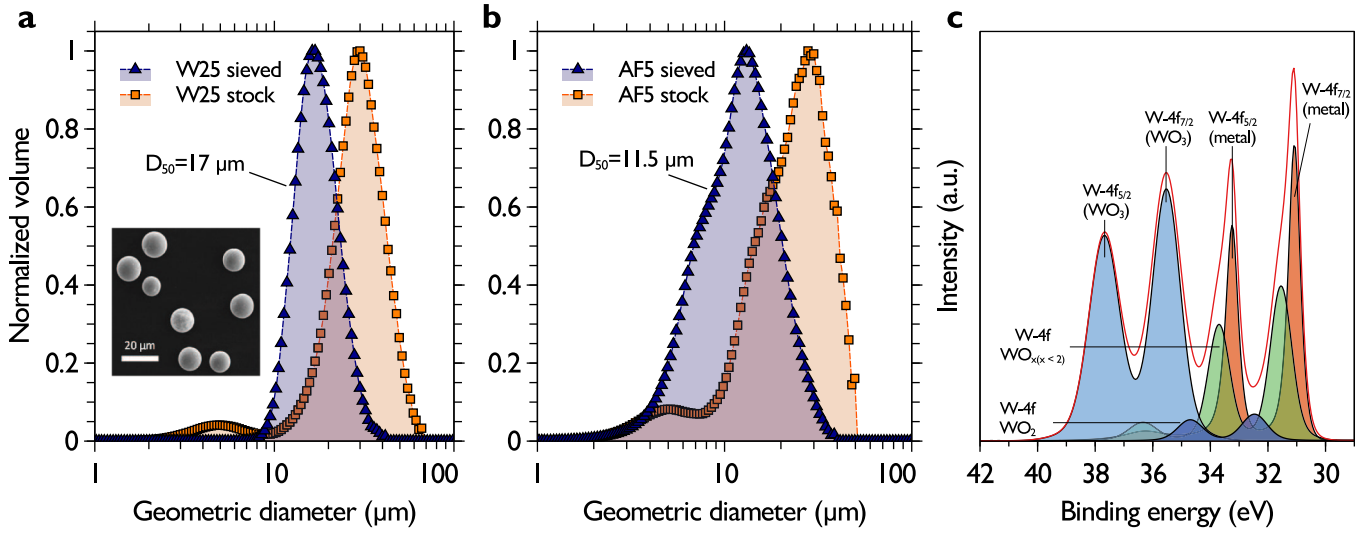

Fig. 3. a Particle size distributions of the Tekna W25 powder before and after sieving. Insert: SEM micrographs of spherical tungsten particles constituting the W25 sieved powder. **b** Particle size distributions of the AF5 tungsten powder before and after sieving. **c** XPS spectrum of tungsten 4f-level showing a large amount of tungsten oxide on the surface of the particles.

should be considered as an estimation regarding the hypothesis made with the core/shell model and the sensitivity of the density measurement method. To complete the characterization of the physical properties of the sieved W25 and AF5 powders, the specific surface areas (SSA) were measured with BET (Brunauer, Emmet and Teller) method. Measurements were performed by nitrogen adsorption using a BET COULTER SA3100 instrument. Prior to the measurement, sample outgassing was performed at 120 °C during 90 min under helium gas flow to remove any adsorbed layer at the surface of the particles. Results obtained with this technique gave SSA of 0.024 ± 0.01 $m^2.g^{-1}$ for the W25 powder and 0.067 ± 0.01 $m^2.g^{-1}$ for the AF5 powder. These values are close to the simple geometric calculation of the SSA for spherical particles indicating that porosity at the surface of the particles is almost absent.

3.2. Loading procedure

Once the tungsten powder was sieved and characterized in terms of particle size distribution and surface composition, it was submitted to a gas loading procedure using tritium. Tritium (T_2) was purchased from TRITEC (purity 99%). The exposure of a material to a hydrogen atmosphere at high temperature induces an equilibrium between the gas and the solid phases. This leads to a thermally activated diffusion of the hydrogen in the bulk of the material (in the lack of other reactions, hydride formation for instance). The method previously developed at the CEA/Joliot tritium lab (see [41;43]) is used in this study. It is a two steps process. First, to avoid cross reaction and barrier effect of the native oxide film, W particles are exposed to a reducing atmosphere of H_2. The W powder is annealed at 743 K for 2 h in a dry hydrogen atmosphere (1.4×10^5 Pa). During the treatment, the desorbed water is collected in a cold trap. Secondly, the small glass vial containing the deoxidized W powder is then loaded with tritium at a pressure of p (T_2) = 0.45×10^5 Pa and sealed in the glove box at room temperature (RT). It is then heated at 743 K for 2 h, the pressure in the vial being 1.1×10^5 Pa of tritium gas. Then, the vial is thermally quenched to the liquid nitrogen temperature to freeze all the detrapping and diffusion processes.

3.3. Tritium absorption/desorption in spherical tungsten particles

Tritium absorption/desorption was measured for a batch of 55 mg of W25 powder and a batch of 42 mg of AF5 powder. Desorption kinetics at room temperature is determined by exposing a 10 mg sample of the powders to air flow (500 ml/min) for several days until reaching a plateau in the cumulated amount of desorbed tritium. The sampled powder is placed in an airtight container with an inlet of clean air from the lab and an outlet to the sampler equipment. The gas released from the powder is swept by the air flow and tritium is trapped in the feeding bottles of a tritium bubbler (MARC 7000 from SDEC France 2010) by means of the bubbling principle. From time to time, the tritiated water contained in the bottles is sampled and measured by liquid scintillation counting (LSC) with a Tri-Carb 2910TR analyzer. These LSC measurements are repeated three times. When the desorbed tritium activity reaches a plateau (see Fig. 4**a** and Fig. 4**b**), the trapped tritium activity in the powders is separately determined by LSC after dissolving small amounts (≈10 mg) of tritiated powder in hydrogen peroxide H_2O_2 solution (wt. 15% in H_2O) with NaOH at 1.5 $mol.l^{-1}$. The dissolution process is controlled during 4 days with stirring periods. Trapped tritium activity measurements are repeated on three different samples from the original batch of powder to check measurement repeatability. The average and standard deviation of these experiments are reported in Fig. 4**a** and Fig. 4**b** for the W25 and AF5 powders, respectively.

For both powders, the main gas-release occurs within 2 days mainly in HTO form. After 13 days of desorption, the whole amount of tritium released by the W25 powder (Fig. 4**a**) is 423 $MBq.g^{-1}$ and the activity of tritium trapped in the tungsten particles is 88.8 $MBq.g^{-1}$. For the second case, after 8 days of desorption, the whole amount of tritium released by the AF5 powder (Fig. 4**b**) is 187 $MBq.g^{-1}$ and the activity of tritium trapped in the tungsten particles is 284 $MBq.g^{-1}$.

Previously, this tritiation procedure has been applied to various types of tungsten particles and to a tungsten massive specimen [41]. The physical characteristics of the different powders are summarized in Table 1. Tungsten nanoparticles produced by planetary ball milling, laser ablation [43] and magnetron sputtering combined with gas aggregation [44] have been tested. The tritium activity trapped in the submicrometer powders and tungsten nanoparticles (NPs) is always above 1 $GBq.g^{-1}$ and a strong dependence with the size of the particles and the specific surface area is visible. Larger metallurgy commercial powders with particle size in the micrometer range have been loaded with tritium the same way and exhibited trapped activity in the range 1–10 $GBq.g^{-1}$.

For the micrometer spherical tungsten particles used in this study, the specific surface area is very low (< 0.1 $m^2.g^{-1}$) and the corresponding tritium trapped activity in the powder is close to the bulk

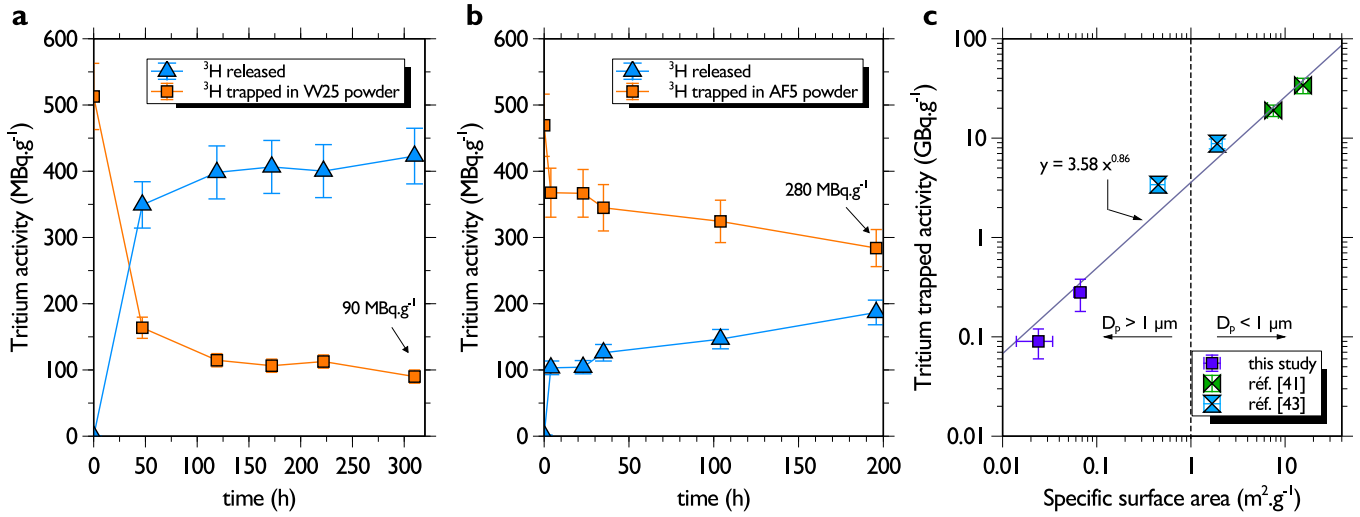

Fig. 4. **a** Total tritium desorption and corresponding amount of trapped tritium for the W25 powder. **b** Total tritium desorption and corresponding amount of trapped tritium for the AF5 powder. **c** Tritium trapped activity in various tungsten powders versus their specific surface area.

trapped activity. From Table 1, it can be noticed that SSA and tritium trapped activities are closely related which emphasizes the hypothesis of a high concentration of hydrogen traps (such as vacancies, dislocations, impurities…) at the surface of the particles [45]. The relation between SSA and trapped activity is plotted in a log–log graph in Fig. 4**c**. For micrometer tungsten particles, specific surface areas are always below 1 $m^2.g^{-1}$ and the tritium trapped activity range between 0.09 $GBq.g^{-1}$ for the spherical particles to 3.4 $GBq.g^{-1}$ for the metallurgy commercial powders. When tungsten particles have sizes in the sub-micrometer range, SSA is greatly increased and tritium trapped activities reach tens of $GBq.g^{-1}$. From the experimental data points presented in Fig. 4**c**, the following linear correlation between the SSA ($m^2.g^{-1}$) and the average tritium trapped activity A_T is found: A_T ($GBq.g^{-1}$) = 3.58 * $SSA^{0.86}$. In the next section, the effect of such tritium activity on the electrostatic self-charging of single tungsten particles is addressed.

4. Electrostatic charging by tritium decay

4.1. Assessment of self-charging rate by Monte-Carlo method

The self-charging rate η (number of positive elementary charges per unit of time) according to a particle diameter is the product of the escape probability of an electron from a β-decay and the particle specific activity (Bq/particle). It is commonly accepted that for an aerosol particle with an embedded strong β emitter, like ^{137}Cs or ^{131}I, the escape probability is close to 1 and the self-charging rate is thus equal to the specific activity. In the case of tritium, the maximal energy of the β-decay is 18.6 keV [46] which corresponds to a maximum path in W of 43 nm [4], thus much smaller than the diameter of the particles. In order to account for the self-charging rate of such particles, it is necessary to estimate the escape probability for one electron with a known energy to get out of the particle. This is investigated using the Geant4 simulation toolkit [47–49] for tungsten particles. The dust particles studied are single spheres with diameters ranging from 0.1 µm to 100 µm. The simulations are realized for pure tungsten particles in vacuum environment following a Monte-Carlo calculation method developed previously [50]. To make a preliminary assessment on the effect of tritium distribution in a particle, two limit cases are considered: 1) tritium is homogeneously distributed in the whole particle; 2) tritium is homogeneously distributed in a 100 nm thick surface layer of the particle. Indeed, case 2 is supported by the fact that presence of oxygen impurities have recently been found in dust collected in the JET tokamak [3,51]. Moreover, a thin oxide layer would confine the trapped tritium in the first hundred nanometres [41] and change the electric properties of the particle from conductive to dielectric [52].

The escape probability of electrons is defined for each particle diameter by the ratio of the electrons that exit the particle by the total number of generated electrons. The tritium β-energy spectrum is used for the energy distribution of electrons and simulation run with about 20,000 tests of one million electrons each. Tritium mass activities of 90 $MBq.g^{-1}$ and 280 $MBq.g^{-1}$ are selected as reported in Section 3. The escape probability of electrons for the two geometries studied is presented in Fig. 5**a**. In case 1, where the electron sources are homogeneously distributed throughout the whole sphere, the electron escape probabilities are 1.1% and 0.7% for the 11.5 µm and 17 µm, respectively. Indeed, for this geometry case, the number of escaping electrons becomes negligible compared to the total number of simulated electrons emission. Thus, the larger is the particle, the lesser the escaping electrons probability. In the case 2, where the electron sources are only distributed in a 100 nm thickness surface layer, the escape probability is found to be close to 20% for the both particle sizes. This means that, the closer is the distribution source to the surface, the more is the escaping probability.

The self-charging rates for the two tritium distribution models and the two specific activities are reported in Fig. 5**b** for particle diameters between 0.1 µm and 100 µm. The models converge towards the same values for small particle diameters (D_p < 400 nm); this behaviour is due to the similar escape probability of electrons. However, for the largest particle diameters (D_p > 1 µm), the self-charging rates increase and diverge between the two tritium distribution models by more than two orders of magnitude. The grey areas in Fig. 5**a** and b represent the geometric median diameters of the two tungsten powders (i.e. 11.5 µm for AF5 and 17 µm for W25) used in the experimental study of Section 3. Escape probability of electrons and self-charging rates for these two powders are summarized in Table 2.

If particles are in vacuum and insulated from the surface where they are deposited (which is a reasonable assumption in presence of a WO_x dielectric layer) MC results can be used to perform analytical calculations of the electrostatic image force acting on the particles. Such calculations are presented in the next section.

4.2. Electrostatic force

By considering the specific activities obtained, i.e. 90 and 280 $MBq.g^{-1}$, one can estimate the time required for the electric charge

Table 1
Summary of tritium loadings in various tungsten powders.

Ref.	[41]	[43]	[44]	[43]	This study	[41]
Fabrication process	Planetary ball milling	Laser ablation	Magnetron sputtering combined with gas aggregation	Metallurgy commercial powder	Plasma spheroidization	Massive specimen mirror polish
Geometric Diameter	20–40 nm	60–80 nm	100–150 nm	0.7–2.9 μm	11.5–17 μm	–
Shape	Polycristalline NPs & aggregates	Heterogeneous NPs & massive droplets	Homogeneous crystalline NPs	Faceted monocrystalline	Spherical	Polycrystalline W sheet
Specific surface area ($m^2.g^{-1}$)	15.5–7.5	43.5	4	1.9–0.45	0.067–0.024	–
Composition	99.9% W	9% W, 91% WO_3	63% W, 37% WO_3	99% W	96% W	99.9% W
Average trapped activity ($GBq.g^{-1}$)	34–19	20.7	1.4	8.8–3.4	0.28–0.09	0.12

carried by the particles (due to self-charging) to become sufficient to develop an electrostatic image force of the same order of magnitude as the van der Waals adhesion force. As a reminder, the van der Waals adhesion force has been measured experimentally by atomic force microscopy technique in previous work [53,54] and is of the order of 10 nN to 20 nN for a micrometer spherical W particle deposited on a W surface with root-mean-square roughness of 700 nm corresponding to average roughness of tokamak tungsten [53]. Due to the presence of the tungsten oxide layer, particles are considered as dielectrics thus without charge leakage to the substrate. As the calculation is intended to represent a real particle of tungsten with an oxide layer, the dielectric constant is expected to be somewhere between the dielectric constant of WO_3 and that of metallic W. In addition, it should be noticed here that calculation is valid under the assumption that electric charge build-up is only due to the β-emission and no neutralization process occurs. Few data can be found in the literature for WO_3 dielectric constant. At ambient air with a temperature of 26 °C, dielectric constant of WO_3 evaporated-films lies between 10 and 30 depending on the thickness of the film [55]. Dielectric constant of such semiconductor is known to be temperature, film thickness and frequency dependent, and as such would be difficult to define exactly.

In the absence of external electrostatic field and neglecting the effect of particle polarization, a dielectric charged particle deposited on a conductive substrate will experience an electrostatic image force towards the substrate expressed by [56]:

$$F_{im} = \alpha(\kappa_s, \kappa_1, \kappa_2)\frac{qq'}{16\pi\varepsilon_0 R_p^2} \quad \text{with} \quad q' = \left(\frac{\kappa_s - \kappa_1}{\kappa_s + \kappa_1}\right)q \tag{1}$$

where q is the charge carried by the particle, q′ is the magnitude of the image charge induced in the substrate, κ_s, κ_1 and κ_2 are the relative dielectric constant of the surface, the environment fluid and the particle, respectively, α is a parameter function of dielectric constants, $\varepsilon_0 = 8.85 \times 10^{-12} F.m^{-1}$ the vacuum permittivity and R_p the particle radius.

For the present case, $\kappa_s \gg \kappa_1$ since we consider the substrate as pure metallic tungsten and $\kappa_1 \approx 1$ for air. From eq.1 one can see that the term $(\frac{\kappa_s - \kappa_1}{\kappa_s + \kappa_1}) \rightarrow 1$ and Eq. (1) becomes:

$$F_{im} = \alpha(\kappa_s, \kappa_1, \kappa_2)\frac{q^2}{16\pi\varepsilon_0 R_p^2} \tag{2}$$

The calculation of α is quite complex but one can find numerically calculated values in the literature (see Ref. [56] for example). If we consider a very thin layer (< 100 nm), dielectric constant of WO_3 is close to 10 [55] and $\alpha \approx 4.8$ in this case. With a tritium specific activity of 90 $MBq.g^{-1}$, a 17 μm tungsten particle placed in a vacuum environment will acquire 3024 positive charges per hour (in the case where tritium is in the 100 nm surface layer) which corresponds to an electrostatic image force of 35 pN, i.e., nearly three hundred times below the van der Waals adhesion force for such particles. In order for the electrostatic image force to reach the same value as the adhesion force, i.e. 10 nN, it is necessary to wait 17 h for the particle to acquire enough charges. The same calculation (time needed to reach electrostatic image force of 10 nN) can be performed for the other configurations considered in this paper, i.e. particle diameter of 11.5 μm and 17 μm and two tritium distributions inside the particles. Results of these calculations are given in Table 2.

For the particle sizes and specific activities used in this study, one find that only few hours are needed to reach an electrostatic image with same magnitude of adhesion force in the case where tritium is trapped in a thin surface layer. Conversely, when the radionuclide is distributed homogeneously in the particle, few days (8–20 days) are required for the self-charging process to induce an electrostatic image force equivalent to the van der Waals force.

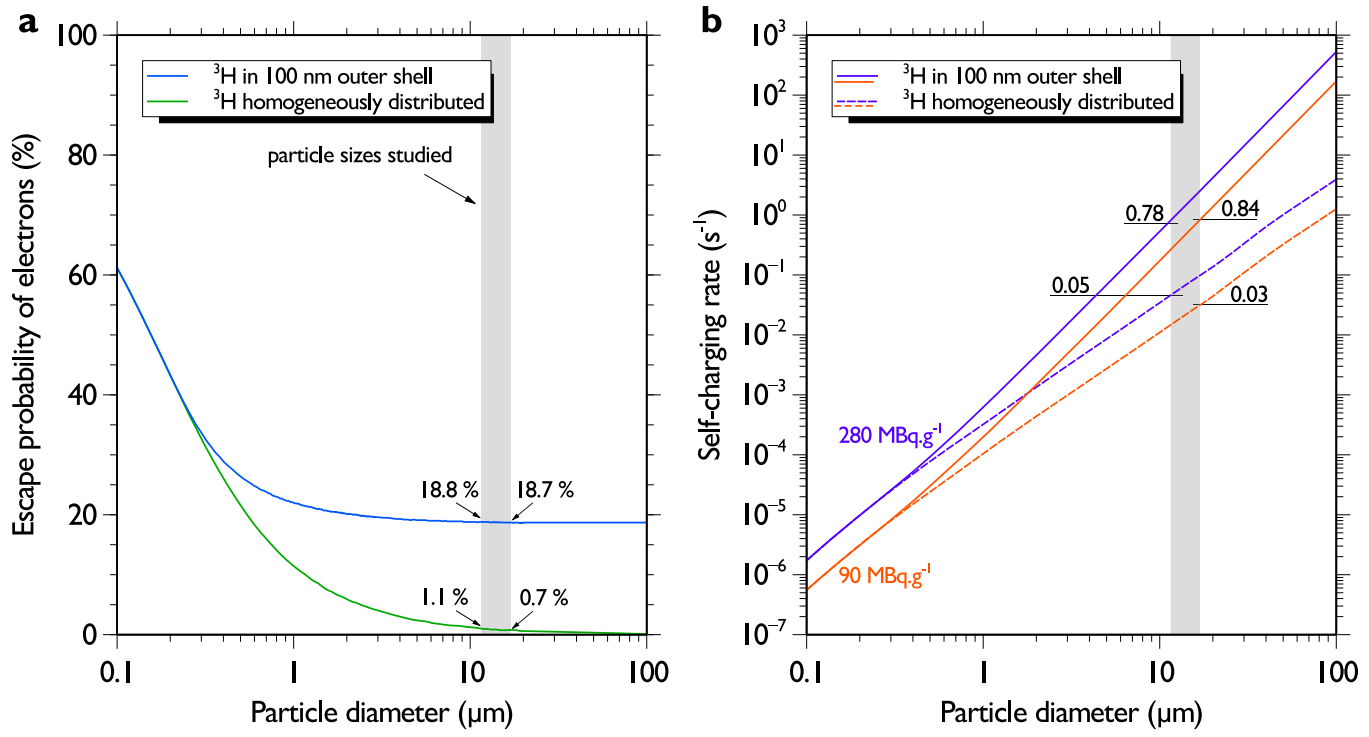

Fig. 5. a Escape probability of electrons in terms of particle diameter for the two geometries considered. **b** Self-charging rate for the two electron sources distribution and the two tritium specific activities in terms of particle diameter.

Table 2
- Monte Carlo simulations results obtained with the 11.5 μm and 17 μm tungsten particles for the two cases considered, i.e., tritium distributions in the particles are homogeneous or in a 100 nm outer shell.

	^{3}H homogeneously distributed		^{3}H in 100 nm outer shell	
Particle diameter (μm)	11.5	17	11.5	17
^{3}H mass activities (MBq.g^{-1})	280	90	280	90
Escape probability of electrons (%)	1.1	0.7	18.8	18.7
Self-charging rate η (s^{-1})	0.05	0.03	0.78	0.84
Time (in hours) needed to reach electrostatic image force of 10 nN	193	475	12	17

5. Conclusion

The paper presented complementary approaches based on experimental and numerical works to address the behavior of tokamak-relevant tungsten particles loaded with tritium. First of all, sampling of particles inside the WEST tokamak was realized thanks to an *in situ* particle collection system called Duster Box. This innovative method allowed to identify various types of tungsten particles among them spherical shaped micro-particles between 5 μm and 30 μm in diameter. Based on these results a surrogate tungsten powder with similar morphology has been obtained by spheroidization process. The tritium retention capacity of this tungsten powder was measured and specific activities of 90 MBq.g^{-1} and 280 MBq.g^{-1} were obtained for spherical particles with 17 μm and 11.5 μm median diameters, respectively. Such tritium specific activities are one to two orders of magnitude below specific activities obtained for sub-micrometer tungsten particles obtained with other techniques but are of the same order of magnitude as specific activities of 6–750 MBq.g^{-1} recently found in dust recovered from JET-ILW [57]. In addition, the strong influence of specific surface area of the particles is discussed and tritium trapped activity above 1 GBq.g^{-1} is systematically found for tungsten powders with specific surface area above 1 m^2.g^{-1}. Considering such tritium activities trapped in the particles, MC simulations have been performed to estimate the electrostatic self-charging rates and the corresponding electrical charge carried by the radioactive tungsten dust. Based on the tritium inventory found in the 17 μm and 11.5 μm particles, simulation results gave self-charging rates of 2988 and 3024 elementary charges per hour, respectively. With such self-charging rates, analytical calculation show that electrostatic image forces on the particles could exceed the magnitude of van der Waals adhesion forces after few days under vacuum.

CRediT authorship contribution statement

S. Peillon: Investigation, Data curation, Formal analysis, Writing - review & editing. **G. Dougniaux:** Software. **M. Payet:** Investigation. **E. Bernard:** Resources. **G. Pieters:** Supervision. **S. Feuillastre:** Resources. **S. Garcia-Argote:** Investigation. **F. Gensdarmes:** Supervision. **C. Arnas:** Investigation. **F. Miserque:** Investigation. **N. Herlin-Boime:** Investigation. **C. Grisolia:** Supervision. **O. Pluchery:** Supervision.

Declaration of Competing Interest

The authors declare that they have no known competing financial interests or personal relationships that could have appeared to influence the work reported in this paper.

Acknowledgments

This work has been carried out within the framework of the EUROfusion Consortium and has received funding from the EURATOM research and training program 2014–2018 and 2019-2020 under grant agreement No. 633053. The views and opinions expressed herein do not necessarily reflect those of the European Commission. The authors gratefully acknowledge the CEA and WEST team for their help and support for the sampling inside the WEST tokamak.

References

[1] N. Taylor, P. Cortes, Lessons learnt from ITER safety & licensing for DEMO and future nuclear fusion facilities, Fusion Eng. Des. 89 (2014) 1995–2000, https://doi.org/10.1016/j.fusengdes.2013.12.030.
[2] S.I. Krasheninnikov, R.D. Smirnov, D.L. Rudakov, Dust in magnetic fusion devices, Plasma Phys. Controlled Fusion 53 (2011) 083001, , https://doi.org/10.1088/0741-3335/53/8/083001.
[3] T. Otsuka, S. Masuzaki, N. Ashikawa, Y. Hatano, Y. Asakura, T. Suzuki, T. Suzuki, K. Isobe, T. Hayashi, M. Tokitani, Y. Oya, D. Hamaguchi, H. Kurotaki, R. Sakamoto, H. Tanigawa, M. Nakamichi, A. Widdowson, M. Rubel, Tritium retention characteristics in dust particles in JET with ITER-like wall, Nucl. Mater. Energy 17 (2018) 279–283, https://doi.org/10.1016/j.nme.2018.11.001.
[4] C. Grisolia, F. Gensdarmes, S. Peillon, G. Dougniaux, E. Bernard, A. Autricque, G. Pieters, B. Rousseau, S. Feuillastre, S. Garcia-Argote, O. Carvalho, V. Malard, I. George, L. Lebaron-Jacobs, T. Orsiere, C. Uboldi, J. Rose, M. Sanles Sobrido, D. Lambertin, D. Vrel, C. Decanis, K. Liger, T. Acsente, G. Dinescu, Current investigations on tritiated dust and its impact on tokamak safety, Nucl. Fusion 59 (2019) 086061, , https://doi.org/10.1088/1741-4326/ab1a76.
[5] S.-H. Hong, C. Grisolia, P. Monier-Gabet, Investigation of temporal evolution and spatial distribution of dust creation events in DITS campaign using visible CCD cameras in Tore Supra, J. Nucl. Mater. 390–391 (2009) 100–102, https://doi.org/10.1016/j.jnucmat.2009.01.120.
[6] C. Grisolia, S. Rosanvallon, A. Loarte, P. Sharpe, C. Arnas, From eroded material to dust: An experimental evaluation of the mobilised dust production in Tore Supra, J. Nucl. Mater. 390–391 (2009) 53–56, https://doi.org/10.1016/j.jnucmat.2009.01.045.
[7] M.I. Guseva, V.M. Gureev, B.N. Kolbasov, S.N. Korshunov, Y.V. Martynenko, V.B. Petrov, B.I. Khripunov, Subthreshold sputtering at high temperatures, JETP Lett. 77 (2003) 362–365, https://doi.org/10.1134/1.1581961.
[8] J. Winter, Dust in fusion devices—a multi-faceted problem connecting high- and low-temperature plasma physics, Plasma Phys. Controlled Fusion 46 (2004) B583–B592, https://doi.org/10.1088/0741-3335/46/12B/047.
[9] T. Acsente, R.F. Negrea, L.C. Nistor, C. Logofatu, E. Matei, R. Birjega, C. Grisolia, G. Dinescu, Synthesis of flower-like tungsten nanoparticles by magnetron sputtering combined with gas aggregation, Eur. Phys. J. D 69 (2015), https://doi.org/10.1140/epjd/e2015-60097-4.
[10] N. Klimov, V. Podkovyrov, A. Zhitlukhin, D. Kovalenko, J. Linke, G. Pintsuk, I. Landman, S. Pestchanyi, B. Bazylev, G. Janeschitz, A. Loarte, M. Merola, T. Hirai, G. Federici, B. Riccardi, I. Mazul, R. Giniyatulin, L. Khimchenko, V. Koidan, Experimental study of PFCs erosion and eroded material deposition under ITER-like transient loads at the plasma gun facility QSPA-T, J. Nucl. Mater. 415 (2011) S59–S64, https://doi.org/10.1016/j.jnucmat.2011.01.013.
[11] M. Laux, W. Schneider, B. Jüttner, S. Lindig, M. Mayer, M. Balden, I. Beilis, B. Djakov, Modification of tungsten layers by arcing, J. Nucl. Mater. 337–339 (2005) 1019–1023, https://doi.org/10.1016/j.jnucmat.2004.10.056.
[12] J. Winter, V.E. Fortov, A.P. Nefedov, Radioactive dust levitation and its consequences for fusion devices, J. Nucl. Mater. 290–293 (2001) 509–512, https://doi.org/10.1016/S0022-3115(00)00524-9.
[13] C.H. Skinner, C.A. Gentile, L. Ciebiera, S. Langish, Tritiated Dust Levitation by Beta Induced Static Charge, U.S. Department of Energy, Princeton University (PPPL—3818), New Jersey, 2003.
[14] A. Grosman, J. Bucalossi, L. Doceul, F. Escourbiac, M. Lipa, M. Merola, M. Missirlian, R.A. Pitts, F. Samaille, E. Tsitrone, The WEST programme: minimizing technology and operational risks of a full actively cooled tungsten divertor on ITER, Fusion Eng. Des. 88 (2013) 497–500, https://doi.org/10.1016/j.fusengdes.2013.02.039.
[15] J. Charuau, Y. Belot, P.h. Cetier, L. Drezet, L. Grivaud, A.T. Peacock, C.H. Wu, Characterization of erosion dust and tritiated products inside the JET vessel after the first tritium experiment, Fusion Technol. (1993) 1700–1703, https://doi.org/10.1016/B978-0-444-89995-8.50333-7.
[16] W.J. Carmack, K.A. McCarthy, D.A. Petti, A.G. Kellman, C.P.C. Wong, Collection and analysis of particulate from the DIII-D Tokamak, Fusion Eng. Des. 39–40 (1998) 477–483, https://doi.org/10.1016/S0920-3796(98)00146-X.
[17] J. Winter, Dust in fusion devices - experimental evidence, possible sources and consequences, Plasma Phys. Controlled Fusion 40 (1998) 1201–1210, https://doi.org/10.1088/0741-3335/40/6/022.
[18] C. Arnas, C. Pardanaud, C. Martin, P. Roubin, G. De Temmerman, G. Counsell, Analyses of dust samples collected in the MAST tokamak, J. Nucl. Mater. 401 (2010) 130–137, https://doi.org/10.1016/j.jnucmat.2010.04.010.
[19] M. Balden, N. Endstrasser, P.W. Humrickhouse, V. Rohde, M. Rasinski, U. von Toussaint, S. Elgeti, R. Neu, the ASDEX Upgrade Team, Collection strategy, inner morphology, and size distribution of dust particles in ASDEX Upgrade, Nucl. Fusion 54 (2014) 073010, , https://doi.org/10.1088/0029-5515/54/7/073010.
[20] A. Widdowson, C.F. Ayres, S. Booth, J.P. Coad, A. Hakola, K. Heinola, D. Ivanova, S. Koivuranta, J. Likonen, M. Mayer, M. Stamp, Comparison of JET main chamber erosion with dust collected in the divertor, J. Nucl. Mater. 438 (2013) S827–S832, https://doi.org/10.1016/j.jnucmat.2013.01.179.
[21] A. Baron-Wiechec, E. Fortuna-Zaleśna, J. Grzonka, M. Rubel, A. Widdowson, C. Ayres, J.P. Coad, C. Hardie, K. Heinola, G.F. Matthews, First dust study in JET with the ITER-like wall: sampling, analysis and classification, Nucl. Fusion 55 (2015) 113033, , https://doi.org/10.1088/0029-5515/55/11/113033.
[22] M. Rubel, A. Widdowson, J. Grzonka, E. Fortuna-Zalesna, S. Moon, P. Petersson, N. Ashikawa, N. Asakura, D. Hamaguchi, Y. Hatano, K. Isobe, S. Masuzaki, H. Kurotaki, Y. Oya, M. Oyaidzu, M. Tokitani, Dust generation in tokamaks: Overview of beryllium and tungsten dust characterisation in JET with the ITER-like wall, Fusion Eng. Des. 136 (2018) 579–586, https://doi.org/10.1016/j.fusengdes.2018.03.027.
[23] J.P. Sharpe, D.A. Petti, A review of dust in fusion devices: Implications for safety and operational performance, Fusion Eng. Des. 63 (2002) 153–163, https://doi.org/10.1016/S0920-3796(02)00191-6.
[24] C.H. Skinner, A. Campos, H. Kugel, J. Leisure, A.L. Roquemore, S. Wagner (Sep 2008). Electrostatic Dust Detection and Removal for ITER (PPPL—4351). United States. https://www.osti.gov/servlets/purl/938797-v7GxuD/.
[25] F.Q.L. Friesen, B. John, C.H. Skinner, A.L. Roquemore, C.I. Calle, Evaluation of an electrostatic dust removal system with potential application in next-step fusion devices, Rev. Sci. Instrum. 82 (2011) 053502, , https://doi.org/10.1063/1.3587619.
[26] N. Endstrasser, V. Rohde, M. Balden, P. Humrickhouse, U. von Toussaint, B.J. Braams, H.-K. Chung, et al., Comparative study of the dust particle population sampled during four consecutive campaigns in full-tungsten ASDEX Upgrade, Phys. Scr. T145 (2011) 014021, , https://doi.org/10.1088/0031-8949/2011/t145/014021.
[27] E. Fortuna-Zaleśna, J. Grzonka, S. Moon, M. Rubel, P. Petersson, A. Widdowson, J.E.T. Contributors, Fine metal dust particles on the wall probes from JET-ILW, Phys. Scr. T170 (2017) 014038, , https://doi.org/10.1088/1402-4896/aa8ddf.
[28] F. Gensdarmes, C. Grisolia, A. Roynette, S. Peillon, T. Gelain, S. Poli, L. Gargiulo, Tore Supra carbon dust resuspension studies, Fusion Eng. Des. 88 (2013) 2684–2687, https://doi.org/10.1016/j.fusengdes.2013.02.148.
[29] A. Rondeau, S. Peillon, A. Roynette, J.-C. Sabroux, T. Gelain, F. Gensdarmes, V. Rohde, C. Grisolia, E. Chassefière, Characterization of dust particles produced in an all-tungsten wall tokamak and potentially mobilized by airflow, J. Nucl. Mater. 463 (2015) 873–876, https://doi.org/10.1016/j.jnucmat.2014.12.051.
[30] S. Peillon, A. Roynette, C. Grisolia, F. Gensdarmes, Resuspension of carbon dust collected in tore supra and exposed to turbulent airflow: controlled experiments and comparison with model, Fusion Eng. Des. 89 (11) (2014) 2789–2796, https://doi.org/10.1016/j.fusengdes.2014.08.004.
[31] T. Gélain, A. Rondeau, S. Peillon, J.C. Sabroux, F. Gensdarmes, CFD modelling of the wall friction velocity field in the ITER tokamak resulting from airflow during a loss of vacuum accident—Consequences for particle resuspension, Fusion Eng. Des. 100 (2015) 87–99, https://doi.org/10.1016/j.fusengdes.2015.04.043.
[32] T. Gelain, F. Gensdarmes, S. Peillon, L. Ricciardi, CFD modelling of particle resuspension in a toroidal geometry resulting from airflows during a loss of vacuum accident (LOVA), Fusion Eng. Des. 151 (2020) 111386, , https://doi.org/10.1016/j.fusengdes.2019.111386.
[33] Y. Otani, N. Namiki, H. Emi, Removal of fine particles from smooth flat surfaces by consecutive pulse air jets, Aerosol Sci. Technol. 23 (1995) 665–673, https://doi.org/10.1080/02786829508965346.
[34] W. John, G. Reischl, Measurements of the filtration efficiencies of selected filter types, Atmos. Environ. 12 (1978) 2015–2019, https://doi.org/10.1016/0004-6981(78)90139-7.
[35] P.A. Baron, P. Kulkarni, K. Willeke (Eds.), Aerosol Measurement: Principles, Techniques, and Applications, 3rd ed., Wiley, Hoboken, N.J., 2011.
[36] J.-C. Soo, K. Monaghan, T. Lee, M. Kashon, M. Harper, Air sampling filtration media: collection efficiency for respirable size-selective sampling, Aerosol Sci. Technol. 50 (2016) 76–87, https://doi.org/10.1080/02786826.2015.1128525.
[37] N. Zíková, J. Ondráček, V. Ždímal, Size-resolved penetration through high-efficiency filter media typically used for aerosol sampling, Aerosol Sci. Technol. 49 (2015) 239–249, https://doi.org/10.1080/02786826.2015.1020997.
[38] M. Firdaouss, C. Desgranges, C. Hernandez, M. Richou, H. Greuner, B. Böswirth, I. Zacharie-Aubrun, T. Blay, J. Bucalossi, M. Missirlian, F. Samaille, E. Tsitrone, Overview of the different processes of tungsten coating implemented into WEST tokamak, Fusion Eng. Des. 124 (2017) 207–210, https://doi.org/10.1016/j.fusengdes.2017.02.087.
[39] R. Behrisch, Contribution of the different erosion processes to material release from the vessel walls of fusion devices during plasma operation, Contrib. Plasma Phys. 42 (2002) 431–444, https://doi.org/10.1002/1521-3986(200204)42:2/4<431::AID-CTPP431>3.0.CO;2-8.2.
[40] X.-L. Jiang, M. Boulos, Induction plasma spheroidization of tungsten and molybdenum powders, Trans. Nonferr. Metals Soc. Chn. 16 (1) (2006) 13–17, https://doi.org/10.1016/S1003-6326(06)60003-4.
[41] A. El-Kharbachi, J. Chêne, S. Garcia-Argote, L. Marchetti, F. Martin, F. Miserque, D. Vrel, M. Redolfi, V. Malard, C. Grisolia, B. Rousseau, Tritium absorption/desorption in ITER-like tungsten particles, Int. J. Hydrogen Energy 39 (2014) 10525–10536, https://doi.org/10.1016/j.ijhydene.2014.05.023.
[42] F.Y. Xie, L. Gong, X. Liu, Y.T. Tao, W.H. Zhang, S.H. Chen, H. Meng, J. Chen, XPS studies on surface reduction of tungsten oxide nanowire film by Ar+ bombardment, J. Electron Spectrosc. Relat. Phenom. 185 (2012) 112–118, https://doi.org/10.

1016/j.elspec.2012.01.004.
[43] E. Bernard, P. Delaporte, F. Jambon, B. Rousseau, C. Grisolia, D. Chaudanson, S. Nitsche, Tungsten dust in fusion tokamaks: relevant dust laser production, characterization and behaviour under tritium loading, Phys. Scr. T167 (2016) 014071, , https://doi.org/10.1088/0031-8949/T167/1/014071.
[44] E. Bernard, R. Sakamoto, E. Hodille, A. Kreter, E. Autissier, M.-F. Barthe, P. Desgardin, T. Schwarz-Selinger, V. Burwitz, S. Feuillastre, S. Garcia-Argote, G. Pieters, B. Rousseau, M. Ialovega, R. Bisson, F. Ghiorghiu, C. Corr, M. Thompson, R. Doerner, S. Markelj, H. Yamada, N. Yoshida, C. Grisolia, Tritium retention in W plasma-facing materials: impact of the material structure and helium irradiation, Nucl. Mater. Energy 19 (2019) 403–410, https://doi.org/10.1016/j.nme.2019.03.005.
[45] E.A. Hodille, E. Bernard, S. Markelj, J. Mougenot, C.S. Becquart, R. Bisson, C. Grisolia, Estimation of the tritium retention in ITER tungsten divertor target using macroscopic rate equations simulations, Phys. Scr. T170 (2017) 014033, , https://doi.org/10.1088/1402-4896/aa8787.
[46] M.-M. Bé, V. Chisté, C. Dulieu, X. Mougeot, E. Browne, V. Chechev, Table of Radionuclides (Comments on evaluation), Bureau International des Poids et Mesures, Sèvres, 2010.
[47] S. Agostinelli, et al., 4 – A simulation toolkit, Nucl. Instrum. Methods Phys. Res. Sect. A 506 (2003) 250–303, https://doi.org/10.1016/S0168-9002(03)01368-8.
[48] J. Allison, et al., Geant4 developments and applications, IEEE Trans. Nucl. Sci. 53 (1) (2006) 270–278, https://doi.org/10.1109/TNS.2006.869826.
[49] J. Allison, et al., Recent developments in Geant 4, Nucl. Instrum. Meth. A 835 (2016) 186–225, https://doi.org/10.1016/j.nima.2016.06.125.
[50] G. Dougniaux, M. Sow, S. Peillon, C. Grisolia, F. Gensdarmes, Monte-Carlo simulations of electrostatic self-charging of tritiated tungsten and beryllium particles, J. Phys. Conf. Ser. 1322 (2019) 012027, , https://doi.org/10.1088/1742-6596/1322/1/012027.
[51] M. Rubel, A. Widdowson, E. Fortuna-Zaleśna, C. Ayres, M. Berry, M. Burford, S. Collins, et al., Search for mobilised dust during operations with equipment for remote handling in JET with ITER-like wall, Phys. Scr. T171 (2020) 014048, , https://doi.org/10.1088/1402-4896/ab4fcf.
[52] S. Peillon, M. Sow, C. Grisolia, F. Miserque, F. Gensdarmes, Mobilization of tungsten dust by electric forces and its bearing on tritiated particles in the ITER tokamak, J. Electrostat. 88 (2017) 111–115, https://doi.org/10.1016/j.elstat.2017.01.020.
[53] A. Autricque, F. Gensdarmes, S. Peillon, M. Sow, C. Grisolia, Adhesion force of W dust on tokamak W plasma-facing surfaces: The importance of the impact velocity, Nucl. Mater. Energy 18 (2019) 345–349, https://doi.org/10.1016/j.nme.2019.02.001.
[54] S. Peillon, A. Autricque, M. Redolfi, C. Stancu, F. Gensdarmes, C. Grisolia, O. Pluchery, Adhesion of tungsten particles on rough tungsten surfaces using Atomic Force Microscopy, J. Aerosol Sci. 137 (2019) 105431, , https://doi.org/10.1016/j.jaerosci.2019.105431.
[55] K. Kant, P. Kant, R. Srivastava, Dielectric properties of vacuum-evaporated films of tungsten oxide, Thin Solid Films 30 (1975) 319–323, https://doi.org/10.1016/0040-6090(75)90096-6.
[56] Thomas B. Jones, Electromechanics of Particles, Cambridge Univ, Press, 1995.
[57] N. Ashikawa, Y. Torikai, N. Asakura, T. Otsuka, A. Widdowson, M. Rubel, M. Oyaizu, M. Hara, S. Masuzaki, K. Isobe, Y. Hatano, K. Heinola, A. Baron-Wiechec, S. Jachmich, T. Hayashi, Determination of retained tritium from ILW dust particles in JET, Nucl. Mater. Energy 22 (2020) 100673, , https://doi.org/10.1016/j.nme.2019.100673.